

N,N-Dimethylformamide Solvent-Assisted Hydrothermal Deposition for Semitransparent Sb₂(S, Se)₃ Solar Cells

M. YAO, Y. CHEN, J. AN, Y. RONG AND Y. WU*

Tiangong University, School of Physical Science and Technology, No. 399, Binshui West Road, Xiqing District, 300387, Tianjin, China

Doi: [10.12693/APhysPolA.147.38](https://doi.org/10.12693/APhysPolA.147.38)

*e-mail: wuyizhi@tiangong.edu.cn

Antimony selenosulfides (Sb₂(S, Se)₃) has garnered significant attention due to its exceptional optoelectronic properties. The quality of the Sb₂(S, Se)₃ thin film is pivotal for its role as the light-absorbing layer in solar cells and directly impacts device performance. This study depicts for the first time the use of *N,N*-dimethylformamide as an assisting solvent in the hydrothermal deposition process for producing semitransparent solar cells based on Sb₂(S, Se)₃ thin films. Comparative analysis with the traditional hydrothermal deposition method using water as the sole solvent reveals a substantial reduction in surface pinholes of the Sb₂(S, Se)₃ thin film, thereby mitigating current leakage resulting from direct contact between the electron transport layer and electrode. X-ray diffraction characterization demonstrates enhanced crystallinity with [021] orientation in the improved Sb₂(S, Se)₃ thin film, facilitating improved carrier transport. Furthermore, the dark *J-V* curve reveals that the reverse saturation current of the Sb₂(S, Se)₃ solar cell with the traditional hydrothermal method is 3.45×10^{-6} mA/cm², whereas for the enhanced Sb₂(S, Se)₃ solar cell, it is 4.65×10^{-7} mA/cm², indicating reduced carrier trapping by defects. These findings reveal that the fill factor of devices obtained through solvent-assisted hydrothermal deposition method with *N,N*-dimethylformamide as an assisting solvent increased from 35.06% to 40.96% and achieved the power conversion efficiency of 3.23%, representing a 50% improvement of the power conversion efficiency over those obtained through traditional hydrothermal deposition without any assisting solvent. The average visible light transmittance was about 9.17%.

topics: *N,N*-dimethylformamide, solvent-assisted hydrothermal deposition, Sb₂(S, Se)₃, semitransparent solar cells

1. Introduction

The advent of industrialization has led to the proliferation of glass skyscrapers, which is expected to increase energy consumption within buildings. Photovoltaic technology directly converts sunlight energy into electric energy [1]. Therefore, the development of transparent photovoltaics (TPVs) offers an effective solution for balancing energy conversion and lighting requirements within architectural structures [2]. Antimony selenosulfides (Sb₂(S, Se)₃), including antimony selenide (Sb₂Se₃) and antimony sulfide (Sb₂S₃), have attracted significant attention due to their excellent optoelectronic properties, such as high carrier mobility, high light absorption coefficient ($> 10^5$ cm⁻¹), and long-term stability [3, 4]. On the one hand, Sb₂S₃ and Sb₂Se₃ (shortly written Sb₂S(e)₃ or Sb₂(S, Se)₃) possess a one-dimensional (1D) crystal structure composed of infinite (Sb₄S(e)₆)_n ribbons connected by strong covalent Sb-S(e) bonds along the [001] direction and weak van der Waals forces along the [010] and [100] directions [5, 6]. This results in highly anisotropic carrier transport within the Sb₂S(e)₃ crystal, with electrical conductivity along the $[hkl]$

direction being 100 times higher than that along the $[hk0]$ direction, and even 1000 times higher along the [001] direction [7]. Therefore, the devices are expected to yield outstanding performance if the growth orientation of the Sb₂S(e)₃ crystal is along the advantageous $[hk1]$ direction [8]. On the other hand, owing to similar crystal structures between Sb₂S₃ and Sb₂Se₃, the band gap of Sb₂(S_{1-x}Se_x)₃ ($0 \leq x \leq 1$) can be continuously tuned from 1.7 to 1.1 eV by varying the Se/S atomic ration [9], thereby facilitating gradient band gap design to effectively enhance device performance [10–12]. With these distinctive characteristics, Sb₂(S, Se)₃ holds promise for advancement in semitransparent photovoltaic (ST-PV) applications [4].

The quality of the Sb₂(S, Se)₃ thin film as the absorber layer is crucial for device performance. Conditions conducive to enhancing device efficiency include favorable crystal orientation, high crystallinity, and well-defined morphology [9, 13]. Huang et al. [14] employed (NH₄)₂S to facilitate hydrothermal sulfidation, thereby improving the crystallinity of Sb₂S₃ thin films and yielding an efficiency of 6.92%. Tang et al. [9] utilized potassium antimony tartrate (KSbC₄H₄O₇), sodium thiosulfate (Na₂S₂O₃), and selenourea (SeC(NH₂)₂) as

sources of Sb, S, and Se, respectively, to prepare precursor solutions and achieved a photoconversion efficiency exceeding 10% via hydrothermal method, marking a significant milestone in the development of $\text{Sb}_2(\text{S, Se})_3$ film solar cells. Based on this work, Chen et al. [15] introduced ethanol as an assisting solvent, which improved the morphology and crystalline quality of the films while reducing defect density. This method led to an increase in the power conversion efficiency (PCE) of 10.75%. However, the majority of high-performance devices [16–19] incorporating the aforementioned technologies utilize relatively thick gold (~ 100 nm) as the counter electrode, and the cost of vacuum deposition for gold electrodes is substantial (~ 100 USD/m²). Consequently, Kumar et al. [13] used carbon/silver electrodes as the counter electrode, with an FTO/TiO₂/Sb₂S₃/CuSCN/C/Ag structure (FTO — fluorine-doped tin oxide) to achieve an efficiency of 1.95% along with an average visible light transmittance (AVT) of 26.7%. Building upon this, they employed ultrathin Au layers (~ 10 nm) as counter electrodes alongside CdS as an electron transport layer (ETL) that have achieved efficiencies up to 2.13% with an AVT at 13% [4]. Furthermore, Lee et al. [20] employed the atomic layer deposition (ALD) process for fabricating semitransparent Sb_2S_3 solar cells (ITO/ALD-TiO₂/ALD-Sb₂S₃/P3HT/Au-10 nm), achieving PCE of 3.44% and AVT of 13%, respectively. Zhang et al. [21] employed graphene as the counter electrode, using the structure of FTO/CdS/Sb₂S₃/Spiro-OMeTAD/graphene, and achieved a PCE value of 2.18%. In addition to the above methods, there is still room to further optimize solar cells by using interface engineering and modifying the structure to create cells that are able to harvest the light better [22]. However, the certified PCE of perovskite solar cells (PSCs) has reached 26.7% [23]; compared to this, the PCE of semitransparent $\text{Sb}_2(\text{S, Se})_3$ (ST- $\text{Sb}_2(\text{S, Se})_3$) solar cells remains relatively low. Therefore, optimizing the quality of the $\text{Sb}_2(\text{S, Se})_3$ films and enhancing device performance are still the focus of current research.

This paper introduces for the first time a novel approach for the production of $\text{Sb}_2(\text{S, Se})_3$ thin films through the utilization of *N, N*-dimethylformamide (DMF) as an assisting solvent in a solvent-assisted hydrothermal deposition (SHD) process. DMF exhibits a lower capacity to dissolve $\text{KSbC}_4\text{H}_4\text{O}_7$ compared to water. During the hydrothermal process, the solubility of $\text{KSbC}_4\text{H}_4\text{O}_7$ in the solvent gradually increases with the rise in temperature, and the deposition of $\text{Sb}_2(\text{S, Se})_3$ films occurs in the process of maintaining or reducing the temperature of the solution. Hence, the solubility gap of the solute within the solution dictates the deposition rate of the thin film onto the substrate. When water is the sole solvent, the hydrothermal deposition rate in water-based

solution is relatively faster due to its stronger ability to dissolve $\text{KSbC}_4\text{H}_4\text{O}_7$ compared to DMF. Conversely, the use of DMF as the solvent results in a relatively slower rate of hydrothermal deposition, which is useful for crystallization. Based on the structure of FTO/CdS/Sb₂(S, Se)₃/Au (~ 10 nm), $\text{KSbC}_4\text{H}_4\text{O}_7$, $\text{Na}_2\text{S}_2\text{O}_3$, and sodium selenosulfate (Na_2SeSO_3) are used as sources of Sb, S, and Se, respectively. This method not only enhances the crystallinity of $\text{Sb}_2(\text{S, Se})_3$ but also reduces the number of pinholes on the film surface, thereby improving the quality of the film. The champion photovoltaic device efficiency reaches 3.23%, which is 50% higher than that achieved by the traditional hydrothermal deposition (HD) process without using any assisting solvents. Additionally, it has an AVT value of 9.17% and a fill factor (FF) that increases from 35.06% to 40.96%.

2. Experimental setup

Preparation of Na_2SeSO_3 : 5.042 g of anhydrous sodium sulfite (Na_2SO_3) (98.0%, Macklin) and 0.632 g of selenium powder (Se) (99.9%, Aladdin) are weighed and then 80 mL of deionized water are added. The mixture is stirred with a stirring rod for 10 min, and the contents are transferred into a tightly sealed 100 mL autoclave Teflon tank. The sealed reaction vessel is placed in a 135°C oven and heated for 5 h. It is allowed to cool naturally, and then the autoclave Teflon tank is opened. The complete dissolution of selenium powder results in a colorless, clear, and transparent solution. The solution is transferred to an amber glass bottle and stored in a dark place. The concentration of the obtained sodium selenite solution is 0.1 M.

Preparation of semitransparent $\text{Sb}_2(\text{S, Se})_3$ thin films by SHD: Water serves as the primary solvent, while DMF ($\geq 99.5\%$, Tianjin Beichen Fangzheng Reagent Factory) acts as an assisting solvent. The $\text{Sb}_2(\text{S, Se})_3$ thin films are hydrothermally deposited on a CdS electron transport layer. The sources of Sb, S, and Se are $\text{KSbC}_4\text{H}_4\text{O}_7 \cdot 0.5\text{H}_2\text{O}$ ($\geq 99.0\%$, Sinopharm Group Chemical Reagent Co., Ltd.), $\text{Na}_2\text{S}_2\text{O}_3 \cdot 5\text{H}_2\text{O}$ (99%, Aladdin), and Na_2SeSO_3 , respectively. Firstly, 50 mM $\text{KSbC}_4\text{H}_4\text{O}_7 \cdot 0.5\text{H}_2\text{O}$ is dissolved in 40 mL deionized water and stirred until complete dissolution. Then, 100 mM $\text{Na}_2\text{S}_2\text{O}_3 \cdot 5\text{H}_2\text{O}$ is added and stirred until complete dissolution. Subsequently, 2 mL of the above Na_2SeSO_3 solution is added with stirring until the solution turns pale yellow. During the SHD process, the total volume of solvent remains at 40 mL, with DMF being added last, accounting for 25%, 50%, and 75% of the total volume, respectively. The fluorine-doped tin oxide (FTO) glass substrate coated with CdS is then tilted and immersed into the Teflon tank

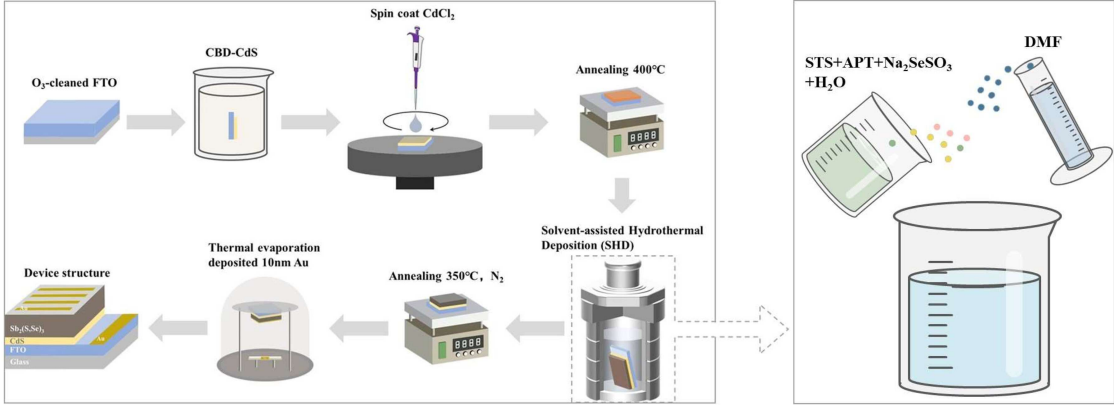


Fig. 1. The SHD preparation process for solar cells based on $\text{Sb}_2(\text{S}, \text{Se})_3$ films. During the solution deposition process, DMF is used as an assisting solvent, $\text{KSbC}_4\text{H}_4\text{O}_7 \cdot 0.5\text{H}_2\text{O}$ (APT), $\text{Na}_2\text{S}_2\text{O}_3 \cdot 5\text{H}_2\text{O}$ (STS), and Na_2SeSO_3 are used as sources of Sb, S, and Se, respectively.

containing the precursor solution and placed in a 120°C oven for 150 min. Following this step, the thin film is recrystallized, and the substrate coated with $\text{Sb}_2(\text{S}, \text{Se})_3$ thin film is placed in an N_2 atmosphere and annealed at 350°C for 10 min. For convenience, the prepared thin films are marked as HD- $\text{Sb}_2(\text{S}, \text{Se})_3$ and SHD- $\text{Sb}_2(\text{S}, \text{Se})_3$ thin films.

Device preparation: All devices are deposited onto fluorine-doped tin oxide (sheet resistance 14Ω , transmittance 83%) glass substrates provided by Guluo Glass Company and undergo ultrasonic cleaning with deionized water, acetone, isopropanol, and ethanol for 40 min each. Hereafter, the FTO is cleaned with a plasma cleaning machine for 15 min. The device adopts an FTO/CdS/ $\text{Sb}_2(\text{S}, \text{Se})_3$ /Au ($\sim 10 \text{ nm}$) configuration, where the CdS layer is chemically deposited at 70°C for 20 min to achieve a thickness of $\approx 80 \text{ nm}$ as ETL. Post-treatment of CdS buffer layer with CdCl_2 : (i) Applying a CdCl_2 (99%, Aladdin) anhydrous methanol saturated solution ($\approx 20 \text{ mg/ml}$) onto the CdS layer using spin-coating, followed by rinsing with methanol; (ii) Placing the treated CdS layer on a hot plate at 400°C and baking in air for 10 min. Subsequently, a 10 nm-thick Au electrode is deposited on the substrate through thermal evaporation, and the effective device area is determined by the aperture of a mask with a diameter of 0.3 cm^2 .

Characterization: The external quantum efficiency (EQE) is measured using the QE system QE-R3011 from Enlitech. The surface and cross-sectional morphology of the $\text{Sb}_2(\text{S}, \text{Se})_3$ film are characterized using a scanning electron microscope (SEM, TESCAN MIRA LMS). The transmission rate of $\text{Sb}_2(\text{S}, \text{Se})_3$ thin films was tested using a UV-visible-near-infrared spectrophotometer (Hitachi, UH4150). The crystal structure of the $\text{Sb}_2(\text{S}, \text{Se})_3$ film is analyzed using an X-ray diffractometer (XRD, Bruker D8 ADVANCE). Under AM1.5 simulation light (AM refers to atmospheric optical quality, 100 mW/cm^2), a solar simulator (Newport, Oriel Sol3A) and a

source meter (Keithley 2400) are used to detect solar cell parameters. Electrochemical impedance spectroscopy measurements use a CHI760E electrochemical station from Shanghai Chenhua Instruments Company, which is set to an initial potential of 0 V and a frequency range of 1 to $1 \times 10^5 \text{ Hz}$.

3. Results and discussion

3.1. Synthesis and characterization of devices

The solution growth deposit method always uses water as the sole solvent, but as a reaction medium, the solvent plays a crucial role. In this study, for the first time, we use water as the main solvent and DMF as the assisting solvent in the hydrothermal process to prepare $\text{Sb}_2(\text{S}, \text{Se})_3$ films, aiming to improve the surface pinholes of $\text{Sb}_2(\text{S}, \text{Se})_3$ films and optimize the orientation of $\text{Sb}_2(\text{S}, \text{Se})_3$ crystals. Figure 1 describes the flowchart of preparing $\text{Sb}_2(\text{S}, \text{Se})_3$ solar cells using this SHD method. More precisely, we use the chemical bath deposition (CBD) method to prepare CdS as the electronic transport layer, which is then spin-coated with a CdCl_2 methanol solution and annealed to mitigate defects. Subsequently, through the SHD method, we fabricate the $\text{Sb}_2(\text{S}, \text{Se})_3$ absorber layer, and after that, we conduct thermal annealing in N_2 . Finally, we use the thermal evaporation method to deposit Au (10 nm) as the counter electrode.

To investigate the optimal amount of assisting solvent in the SHD process, four precursor solutions were formulated by varying the DMF-to-water ratio from 0% (HD) to 25%, 50%, and 75%, while maintaining a constant total solvent volume of 40 mL . To compare the performance of $\text{Sb}_2(\text{S}, \text{Se})_3$ solar cells prepared with different precursor solutions, we prepared 30 solar cells with an area of 0.3 cm^2 and different precursor solution concentrations,

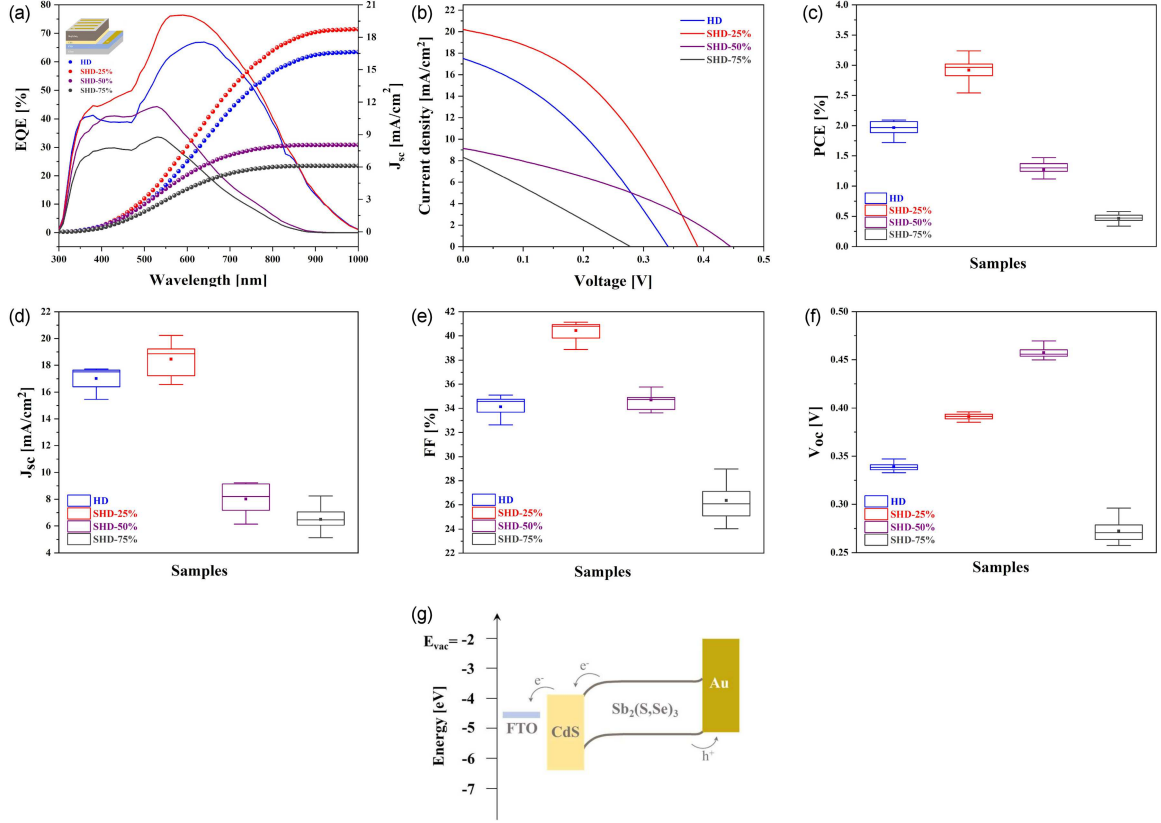


Fig. 2. Characteristics of $\text{Sb}_2(\text{S}, \text{Se})_3$ thin-film solar cells. (a) EQE spectra and the relevant J_{sc} curves of the champion $\text{Sb}_2(\text{S}, \text{Se})_3$ solar cells in each case. (b) J - V curves of the champion $\text{Sb}_2(\text{S}, \text{Se})_3$ solar cells in each case. (c) PCE, (d) J_{sc} , (e) FF, and (f) V_{oc} statistical boxplots of $\text{Sb}_2(\text{S}, \text{Se})_3$ solar cells with different amounts of DMF. (g) Energy level diagram of the $\text{Sb}_2(\text{S}, \text{Se})_3$ solar cell.

respectively, and measured their external quantum efficiency (EQE) and photocurrent density–voltage (J - V) curves (as shown in Fig. 2a–b). Furthermore, the statistical distribution of solar cell parameters for all cells under standard AM 1.5G illumination was analyzed and is presented in Fig. 2c–f. The champion efficiency appears in the sample with 25% DMF, as indicated in Table I, where the open circuit voltage (V_{oc}), short-circuit current density (J_{sc}), and FF are respectively 0.39 V, 20.20 mA/cm^2 , and 40.96%, resulting in a PCE of 3.23%. In addition, the boxplot of PCE values for the champion device, as depicted in Fig. 2c, reveals that PCE is distributed within a narrow range of 2.5–3.5%, which speaks of the repeatability of the device [24]. When water is used as the only solvent for solar cells, the values of V_{oc} , J_{sc} , and FF of the solar cell are 0.34 V, 17.51 mA/cm^2 , and 35.06%, respectively. The PCE of the device is measured to be 2.09%. The addition of DMF enhances the overall performance of the device, primarily due to the contributions of J_{sc} and FF (see Fig. 2d–e). Compared to traditional hydrothermal deposition of $\text{Sb}_2(\text{S}, \text{Se})_3$ devices, when the percentage of DMF is 25%, R_{sh} increases from 120.61 to 289.50 Ω , which may be due to the reduced number of film pinholes

TABLE I

Photovoltaic parameters of devices based on different DMF content.

Device	V_{oc} [V]	J_{sc} [$\frac{\text{mA}}{\text{cm}^2}$]	FF [%]	PCE [%]	R_s [$\frac{\Omega}{\text{cm}^2}$]	R_{sh} [$\frac{\Omega}{\text{cm}^2}$]
HD	0.34	17.51	35.06	2.09	27.16	120.61
SHD-25%	0.39	20.20	40.96	3.23	30.99	289.50
SHD-50%	0.44	9.14	35.76	1.47	42.85	183.96
SHD-75%	0.28	8.25	24.79	0.58	173.91	200.80

after improvement, leading to less leakage. This will be discussed in detail later, and the increase in R_{sh} leads to an increase in FF from 35.06% to 40.96% (Table I) [25], where the enlargement of the FF is one of the main reasons for the enhancement of PCE.

Specifically, when the DMF percentage in the solution reaches 25%, J_{sc} of the test device increases to 20.20 mA/cm^2 (Fig. 2b), while the value calculated based on the EQE result is 18.73 mA/cm^2 (Fig. 2a). The reason for the minor difference between the EQE calculation result and

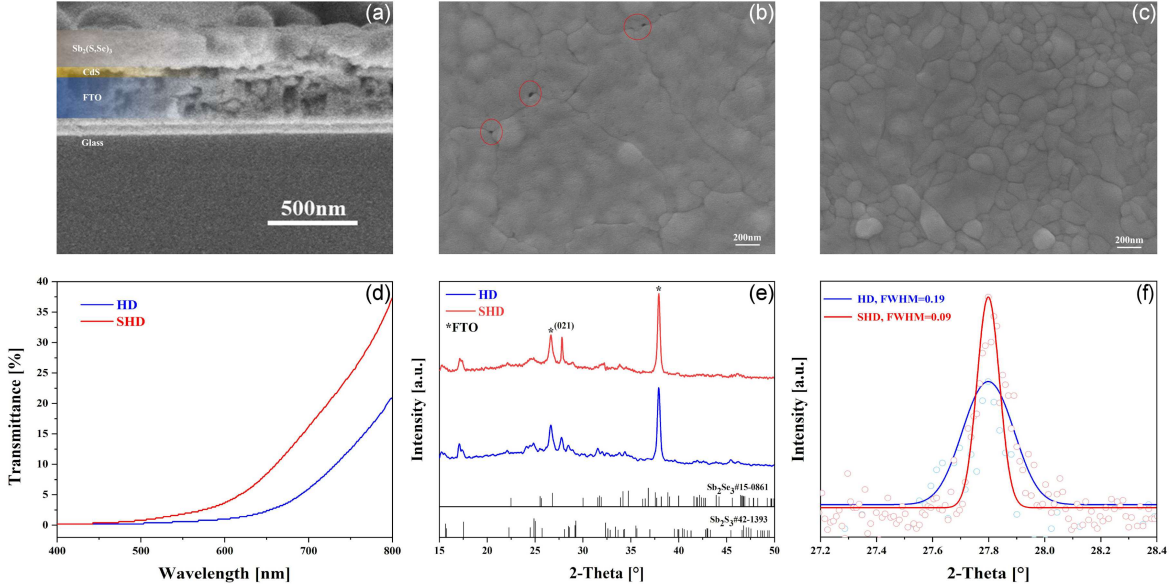


Fig. 3. Basic properties of $\text{Sb}_2(\text{S}, \text{Se})_3$ films. (a) SEM cross-sectional image of SHD- $\text{Sb}_2(\text{S}, \text{Se})_3$ film. (b, c) SEM images (top view) of $\text{Sb}_2(\text{S}, \text{Se})_3$ films based on HD and SHD, respectively. (d) Transmission spectrum of the semitransparent device. (e) XRD spectrum and (f) magnified XRD spectrum of $\text{Sb}_2(\text{S}, \text{Se})_3$ films.

the PCE test result lies in the fact that the EQE test measures only a small region of the active area (0.01 cm^2), while the PCE test assesses the average effect across the entire active area (0.3 cm^2). EQE results show that $\text{Sb}_2(\text{S}, \text{Se})_3$ solar cells with a SHD-25% composition exhibit a higher quantum production rate within the mid to long wave range (450–850 nm) compared to those fabricated using traditional hydrothermal deposition methods, for instance, at a wavelength of 560 nm, the EQE quantum yield of SHD-25% $\text{Sb}_2(\text{S}, \text{Se})_3$ is 76.07%, while that of HD- $\text{Sb}_2(\text{S}, \text{Se})_3$ at the same position is only 62.17%. This suggests that the SHD process enhances interface contact [26], leading to better electron–hole separation at the interface, which is also the reason for the J_{sc} value improvement [27]. As shown in Fig. 2g, at the interface between CdS and $\text{Sb}_2(\text{S}, \text{Se})_3$, the separation of electrons and holes is facilitated by the built-in electric field, which is beneficial to the transport of electrons along the energy band towards the CdS direction, which is also the reason for the improvement of J_{sc} .

Considering that the optimal DMF content is 10 ml, for ease of description, the defaulted volume of DMF in the “SHD” experimental groups is 10 ml, and it is 0 in the “HD” control group.

3.2. Analysis of the properties of $\text{Sb}_2(\text{S}, \text{Se})_3$ films

In order to gain a deeper understanding of the impact of DMF on $\text{Sb}_2(\text{S}, \text{Se})_3$ films, solar cells were fabricated using the SHD process and

subsequently subjected to scanning electron microscope (SEM) analysis for their sectional structure (as depicted in Fig. 3a). The respective film thicknesses of CdS and $\text{Sb}_2(\text{S}, \text{Se})_3$ are 80 nm and 220 nm. Figure 3d illustrates the transmittance curve of the device (FTO/CdS/ $\text{Sb}_2(\text{S}, \text{Se})_3$ /Au), with HD- $\text{Sb}_2(\text{S}, \text{Se})_3$ and SHD- $\text{Sb}_2(\text{S}, \text{Se})_3$ exhibiting AVT values of 9.17% and 4.07%, respectively. PCE and AVT are mostly inversely related. The SHD- $\text{Sb}_2(\text{S}, \text{Se})_3$ solar cell exhibits a 50% higher efficiency (PCE = 3.23%) compared to the HD- $\text{Sb}_2(\text{S}, \text{Se})_3$ solar cell (PCE = 2.09%). Subsequently, SEM surface morphology tests were conducted on $\text{Sb}_2(\text{S}, \text{Se})_3$ films produced by both HD and SHD methods. It is evident from the SEM images that there are noticeable pinholes in the HD- $\text{Sb}_2(\text{S}, \text{Se})_3$ film (Fig. 3b), which is destructive for the device performance and stability, possibly leading to current loss and ultimately reducing the performance of the device [27]. In contrast, the surface morphology of the SHD- $\text{Sb}_2(\text{S}, \text{Se})_3$ film was enhanced (Fig. 3c), exhibiting a more compact and uniformly distributed structure, leading to a decrease in the occurrence of pinholes on the surface. The reduction in the occurrence of pinholes serves to mitigate potential current leakage arising from direct contact between the ETL and the electrode [28]. Consequently, the current loss is reduced, and J_{sc} is increased. The short-circuit current density (J_{sc}) of the SHD- $\text{Sb}_2(\text{S}, \text{Se})_3$ sample is 20.20 mA/cm^2 , while that of HD- $\text{Sb}_2(\text{S}, \text{Se})_3$ is only 17.51 mA/cm^2 . We believe that the reduction in the number of pinholes is one of the main reasons for the enhancement of J_{sc} in the SHD- $\text{Sb}_2(\text{S}, \text{Se})_3$ solar cell.

X-ray diffraction (XRD) was employed to analyze the crystal structures of $\text{Sb}_2(\text{S, Se})_3$ thin films deposited by HD and SHD processes (Fig. 3e-f). From the XRD pattern (Fig. 3e), it is evident that the intensity of the peak at [021] for the SHD- $\text{Sb}_2(\text{S, Se})_3$ crystal structure is significantly stronger than that of the HD- $\text{Sb}_2(\text{S, Se})_3$ crystal structure, indicating an enhancement in film crystallinity [29]. The enhancement of crystallinity in the [021] orientation is believed to be favorable for carrier transmission because the grains in the [021] orientation are composed of tilted one-dimensional $(\text{Sb}_4\text{S}(\text{e})_6)_n$ ribbon structures, where carriers move within the covalent bonds $(\text{Sb}_4\text{S}(\text{e})_6)_n$ during transmission. In contrast, the grains in the $[hk0]$ orientation are made up of horizontal stacks of $(\text{Sb}_4\text{S}(\text{e})_6)_n$ ribbon structures, requiring carriers to jump between ribbons. Therefore, the [021] orientation is considered benign, and the optimization of crystal orientation helps to improve carrier transportation [9], which is also an important reason for the increase in J_{sc} and FF [6, 24]. Furthermore, fitting peak sections (Fig. 3f) at the [021] position ($\theta = 27.77^\circ$) revealed a full width at half maximum (FWHM) value of 0.19 for HD- $\text{Sb}_2(\text{S, Se})_3$ and 0.09 for SHD- $\text{Sb}_2(\text{S, Se})_3$ films, respectively, suggesting a higher degree of crystallization in SHD-prepared films.

To get more information about the microstructure of the films, we have calculated the average crystallite size (D) of the grains in the films, which we estimated from the broadening of the (021) prominent peak with the help of Scherrer's equation

$$D = \frac{0.9\lambda}{\beta \cos(\theta)}, \quad (1)$$

where λ is the X-ray wavelength, β is the full width at half maximum of the diffraction peaks under consideration, and θ is the Bragg angle.

By substituting the FWHM (Fig. 3f) of both peaks into the equation, it can be obtained that the grain size of SHD- $\text{Sb}_2(\text{S, Se})_3$ is larger than that of HD- $\text{Sb}_2(\text{S, Se})_3$. The increased crystallinity and grain size are believed to be able to improve the charge transport [30].

The preferential orientation of crystals is favorable for improving the quality of $\text{Sb}_2(\text{S, Se})_3$ films, making them less defective and of better quality [29].

3.3. Photoelectric performance analysis

To understand the reasons for the enhancement of solar cell performance, we have carried out device tests on carrier transport and combination, as shown in Fig. 4a. The dark $J-V$ curves of both HD- $\text{Sb}_2(\text{S, Se})_3$ and SHD- $\text{Sb}_2(\text{S, Se})_3$ devices were examined, and the values of reverse saturation current densities (J_0) were extracted from the intercepts of these curves [27]. It is known that the

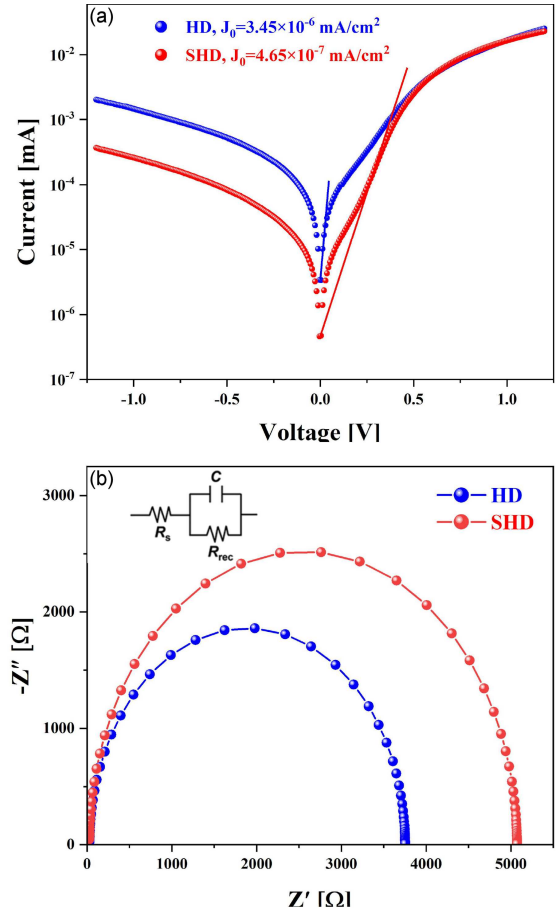


Fig. 4. Carrier transport. (a) The semi-logarithmic dark $J-V$ curve and (b) the Nyquist plot of $\text{Sb}_2(\text{S, Se})_3$ films (inset shows the equivalent circuit diagram).

value of J_0 is determined by internal charge recombination within the device, and its magnitude serves as an indicator for assessing improvements in device performance [31]. The reverse saturation current densities (J_0) of HD- $\text{Sb}_2(\text{S, Se})_3$ and SHD- $\text{Sb}_2(\text{S, Se})_3$ devices are 3.45×10^{-6} mA/cm² and 4.65×10^{-7} mA/cm², respectively. Generally, a lower J_0 value indicates that there are more carriers in transit and fewer are being captured by the defects [32]. Therefore, the reduction in the J_0 value of $\text{Sb}_2(\text{S, Se})_3$ films prepared by the SHD process indicates that SHD plays a positive role in inhibiting carrier recombination, and the increase in V_{oc} can be attributed to the decrease in J_0 [25, 31]. To explore the underlying mechanisms driving the enhanced solar cell performance resulting from the novel strategy proposed in this study, Fig. 4b illustrates the results of the electrochemical impedance spectroscopy (EIS) results of an $\text{Sb}_2(\text{S, Se})_3$ solar cell, in which R_s and R_{rec} denote the charge transfer resistance (R_s) and recombination resistance (R_{rec}), respectively. The value of R_{rec} corresponds to the recombination resistance

TABLE II
EIS parameters of HD and SHD-Sb₂(S, Se)₃ devices.

Samples	R_s [Ω]	R_{rec} [Ω]
HD	29.61	3752.73
SHD	27.40	5071.90

at the interfaces in the device, which is determined by the diameter of the semicircle in the EIS [24]. The charge transfer resistance (R_s) of the SHD-Sb₂(S, Se)₃ device exhibits no significant difference compared to that of the HD-Sb₂(S, Se)₃ device. However, R_{rec} of the SHD-Sb₂(S, Se)₃ device measures 5071.90 Ω , surpassing that of the HD-Sb₂(S, Se)₃ device at 3752.73 Ω (Table II). It indicates that our proposed SHD method may decrease the defects of Sb₂(S, Se)₃ film, because greater R_{rec} indicates the effective inhibition of charge recombination [33].

As shown in Table II, this observation indicates that there are fewer recombinations of carriers at the interface of the SHD-Sb₂(S, Se)₃ solar cell, promoting effective current formation and transport. Consequently, employing the SHD process can effectively reduce the charge transfer barrier to promote the separation and migration of charge carriers, thereby enhancing V_{oc} , FF, and PCE [24].

4. Conclusions

In summary, for the first time, we developed a SHD method using DMF as an assisting solvent to fabricate Sb₂(S, Se)₃ thin films. This method is advantageous for promoting the crystallinity of Sb₂(S, Se)₃ crystals along the [021] orientation, optimizing crystal orientation, reducing the density of pinholes on the surface of Sb₂(S, Se)₃ thin films, improving film morphology, and achieving a record device efficiency of 3.23%. This study presents a novel approach for the fabrication of semitransparent Sb₂(S, Se)₃ solar cells using the SHD method.

Acknowledgments

This work was supported by the National Natural Science Foundation of China (11504264) and the Tianjin Research Innovation Project for Postgraduate Students (2022SKY141).

References

[1] R. Zhou, Z. Yang, J.Z. Xu, G.Z. Cao, *Coord. Chem. Rev.* **374**, 279 (2018).

[2] K. Lee, H.D. Um, D. Choi, J. Park, N. Kim, H. Kim, K. Seo, *Cell Rep. Phys. Sci.* **1**, 24 (2020).

[3] M. Ishaq, H. Deng, S. J. Yuan, H. Zhang, J. Khan, U. Farooq, H.S. Song, J. Tang, *Sol. RRL* **2**, 9 (2018).

[4] P. Kumar, M. Eriksson, D.S. Kharytonau, S.J. You, M.M. Natile, A. Vomiero, *ACS Appl. Energy Mater.* **7**, 1421 (2024).

[5] Y. Zhou, M.Y. Leng, Z. Xia et al., *Adv. Energy Mater.* **4**, 8 (2014).

[6] Y. Zhou, L. Wang, S.Y. Chen et al., *Nat. Photon.* **9**, 409 (2015).

[7] R. Kondrotas, C. Chen, J. Tang, *Joule* **2**, 857 (2018).

[8] Z.Q. Li, X.Y. Liang, G. Li et al., *Nat. Commun.* **10**, 9 (2019).

[9] R.F. Tang, X.M. Wang, W.T. Lian et al., *Nat. Energy* **5**, 587 (2020).

[10] W. Liu, H.T. Li, B. Qiao, S.L. Zhao, Z. Xu, D.D. Song, *Sol. Energy* **233**, 337 (2022).

[11] S.Y. Kuo, M.Y. Hsieh, D.H. Hsieh, H.C. Kuo, C.H. Chen, F.I. Lai, *Int. J. Photoenergy* **2014**, 6 (2014).

[12] J.B. Gong, Y.F. Kong, J.M. Li, K.F. Wang, X.Q. Wang, Z.M. Zhang, Z.J. Ding, X.D. Xiao, *Nano Energy* **62**, 205 (2019).

[13] P. Kumar, S.J. You, A. Vomiero, *J. Mater. Chem. C* **10**, 16273 (2022).

[14] Y.Q. Huang, H.H. Gao, X.Q. Peng, G. Wang, P. Xiao, B. Che, R.F. Tang, C.F. Zhu, T. Chen, *Sol. RRL* **7**, 8 (2023).

[15] X.L. Chen, B. Che, Y.Q. Zhao et al., *Adv. Energy Mater.* **13**, 10 (2023).

[16] R.F. Tang, X.M. Wang, C.H. Jiang, S. Li, W.F. Liu, H.X. Ju, S.F. Yang, C.F. Zhu, T. Chen, *ACS Appl. Mater. Interfaces* **10**, 30314 (2018).

[17] J. Han, X.Y. Pu, H. Zhou et al., *ACS Appl. Mater. Interfaces* **12**, 44297 (2020).

[18] C.H. Jiang, R.F. Tang, X.M. Wang, H.X. Ju, G.L. Chen, T. Chen, *Sol. RRL* **3**, 8 (2019).

[19] J. Han, S.J. Wang, J.B. Yang, S.H. Guo, Q. Cao, H.J. Tang, X.Y. Pu, B.Y. Gao, X.H. Li, *ACS Appl. Mater. Interfaces* **12**, 4970 (2020).

[20] S.J. Lee, S.J. Sung, K.J. Yang, J.K. Kang, J.Y. Kim, Y.S. Do, D.H. Kim, *ACS Appl. Energy Mater.* **3**, 12644 (2020).

[21] J.W. Zhang, W.T. Lian, Y.W. Yin, X.M. Wang, R.F. Tang, C. Qian, X.J. Hao, C.F. Zhu, T. Chen, *Sol. RRL* **4**, 6 (2020).

[22] Z. Yang, W.H. Zhang, *Chin. J. Catal.* **35**, 983 (2014).

- [23] M.A. Green, E.D. Dunlop, M. Yoshita et al., *Prog. Photovolt.* **32**, 425 (2024).
- [24] Y. Mao, L. Huang, W.G. Zeng, F.Y. Wu, L.Q. Yao, L.M. Lin, J.M. Zhang, J.M. Li, G.L. Chen, *Chem. Eng. J.* **446**, 10 (2022).
- [25] Y.L. Pan, X.B. Hu, Y.X. Guo et al., *Adv. Funct. Mater.* **31**, 9 (2021).
- [26] J.M. Li, Y.Q. Zhao, C. Li, S.Y. Wang, X.L. Chen, J.B. Gong, X.M. Wang, X.D. Xiao, *Adv. Sci.* **9**, 10 (2022).
- [27] M. Azam, Y.D. Luo, R. Tang et al., *ASC Appl. Mater. Interfaces* **14**, 4276 (2022).
- [28] Y.Q. Zhao, S.Y. Wang, C. Li et al., *Energy Environ. Sci.* **15**, 5118 (2022).
- [29] W.L. Shao, H.B. Wang, F.H. Ye et al., *Energy Environ. Sci.* **16**, 252 (2023).
- [30] C.H. Jiang, R.F. Tang, X.M. Wang, H.X. Ju, G.L. Chen, T. Chen, *Sol. RRL* **3**, 8 (2019).
- [31] X. Jin, Y.A. Fang, T. Salim, M.J. Feng, S. Hadke, S.W. Leow, T.C. Sum, L.H. Wong, *Adv. Funct. Mater.* **30**, 11 (2020).
- [32] C. Liu, Z.X. Pan, K. Shen et al., *J. Energy Chem.* **68**, 521 (2022).
- [33] X.L. Mao, M.R. Bian, C.X. Wang et al., *ACS Appl. Energ. Mater.* **5**, 3022 (2022).